SAND2018-13214B

Chapter 5 - HIGH ENTHALPY EFFECTS ON HYPERSONIC BOUNDARY LAYER TRANSITION

Viola Wartemann, Alexander Wagner
German Aerospace Center (DLR), Institute of Aerodynamics and Flow Technology, Spacecraft Department
GERMANY

Ross Wagnild
Sandia National Laboratories
USA

Fabio Pinna, Fernando Miró Miró
von Karman Institute for Fluid Dynamics, Aeronautics and Aerospace Department
BELGIUM

Hideyuki Tanno
Japan Aerospace Exploration Agency, Kakuda Space Center
JAPAN

Heath Johnson
VirtusAero LLC
USA

5.0 NOMENCLATURE

f	Frequency, kHz
h	Enthalpy, $\mathrm{MJ/kg}$
M	Mach number
N	N-factor
p	Pressure, MPa
q	Flow / material quantity
Re_m	Unit Reynolds number
T	Temperature, K
u, v, w	Velocity in x-, y-, z-direction, $\mathrm{m/s}$
x, y, z	Coordinates, m
α, β	Wave numbers
σ	Growth rate, $1/\mathrm{m}$
ρ	Density, $\mathrm{g/m^3}$

Subscripts

e	Boundary layer edge quantity
w	Wall quantity
∞	Free stream quantity
0	Reservoir quantity

Sandia National Laboratories is a multimission laboratory managed and operated by National Technology & Engineering Solutions of Sandia, LLC, a wholly owned subsidiary of Honeywell International Inc., for the U.S. Department of Energy's National Nuclear Security Administration under contract DE-NA0003525.

Superscripts

$\bar{}$ Base flow quantity
$\tilde{}$ Disturbance flow quantity
$\hat{}$ Eigenfunction

5.1 INTRODUCTION

Laminar to turbulent transition in high speed boundary layers is of high importance for re-entry vehicles since early transition can increase the surface heat transfer by a factor of 3 to 8 [1, 2]. The uncertainty on the transition location usually leads to an oversized thermal protection system, adding extra costs and reducing the payload of a hypersonic system. The second mode instability, commonly referred to as second mode or Mack mode [3], is the dominant boundary layer instability for essentially 2D boundary layers at high local Mach number ($Ma_e > 4$) and/or cold walls [3]. Therefore, the second mode is the main focus of the investigations in this chapter. High speed vehicles and re-entry vehicles operate in a high enthalpy range. In this range, real gas effects occur, which can include molecular rotation, molecular vibration, chemical dissociation and exchange, electronic excitation, radiation and ionization. In this chapter, the high enthalpy effects on second mode instabilities are investigated. The numerical investigations are performed with three different stability codes, which are compared against each other: the NOLOT code of the DLR, the STABL code from VirtusAero and the VESTA code of VKI, which are described in section 5.3.The stability results are compared against low and high enthalpy experiments, which were performed on a blunted 7° half-angle cone model. The two high enthalpy shock tunnels (HEG and HIEST), in which the experiments were conducted, are described in section 5.2. The mean flow as well as the stability calculations themselves are performed with and without real gas effects to isolate the high enthalpy effect on the instability. Currently, the NOLOT stability code is limited to caloric or thermal perfect gas assumptions. Thus, an essential element of this chapter is to assess the effect of real gas effects during the stability analysis.

5.2 GROUND TEST FACILITY AND CONE TEST ARTICLE

The experimental data referred to in the present study were obtained in two free-piston driven reflected shock tunnels, the DLR High Enthalpy Shock Tunnel Göttingen (HEG) [4] and the JAXA High Enthalpy Shock tunnel (HIEST) [5]. Similar test conditions were chosen with respect to unit Reynolds number, Mach number and total enthalpy. Table 5-1 provides a low enthalpy test condition from HEG and two comparable high enthalpy test conditions of both tunnels. The HEG conditions of table 5-1 were derived by nozzle computations using the DLR TAU code [6–8] in combination with a one temperature model, thus, assuming thermal equilibrium, which was shown to be a reasonable approach [9, 10]. The HIEST test conditions were calculated using a two temperature model. As shown in table 5-1 the translational-rotational and vibrational temperatures are almost identical which supports the before mentioned assumption. The model wall temperature for all tests is assumed to be isothermal at 293 K.

All tests were conducted on separate 7° half-angle blunted cones with a nose tip radius of $2.5\,\mathrm{mm}$ and an overall length of about $1\,\mathrm{m}$. Each model was supported by a sting at a nominal angle of attack of $0°$. Further, both models were equipped with thermocouples and PCB flush mounted pressure transducers. The latter transducer

Table 5-1: HEG and HIEST Test Conditions Used in the Present Study.

Condition	HEG-Low-E	HEG-High-E	HIEST-High-E
p_0 [MPa]	7.1	38.8	46.8
T_0 [K]	2680	6690	6370
h_0 [MJ·kg^{-1}]	3.1	11.6	10.9
M_∞ [-]	7.35	6.09	6.05
T_∞ (1T) [K]	264	1268	-
T_{vib} (2T) [K]	-	T_∞	1192
T_{rot} (2T) [K]	-	T_∞	1185
ρ_∞ [g·m^{-3}]	10.7	17.1	19
u_∞ [m·s^{-1}]	2399	4354	4246
Re_m [m^{-1}]	$1.55 \cdot 10^6$	$1.52 \cdot 10^6$	$1.71 \cdot 10^6$

have a response time of $\approx 1\,\mu$s and were used to capture the second mode frequencies for later comparison with stability analysis. On the cone model used in HIEST the PCB transducers were positioned between $0.412\,\mathrm{m}$ to $1.012\,\mathrm{m}$, measured from the sharp tip, with a spacing of $0.04\,\mathrm{m}$ [11]. On the HEG model the PCB transducers were placed at $0.650\,\mathrm{m}$, $0.785\,\mathrm{m}$ and $0.965\,\mathrm{m}$ from the sharp tip [12].

5.3 NUMERICAL METHODS

5.3.1 Mean Flow Solver

The laminar base flows $\bar{q}$, which are required for the stability analysis, are calculated by different CFD solvers, which are not described in detail here. For NOLOT the DLR TAU code is applied, which is a three-dimensional parallel hybrid multi-grid code and has been validated for hypersonic flows (see e.g. [6–8]). The base flow calculations account for real gas effects, based on non-equilibrium gas modeling with 5 species for air: N_2, O_2, NO, N, O. Different assumptions are applied: thermal equilibrium and chemical non-equilibrium (one temperature models) and thermochemical non-equilibrium (two and three temperature model). Constant free stream conditions, which are listed in table 5-1, are used. Additional mean flow calculations with a perfect gas assumption are performed to isolate the real gas effects. Figure 5-1 shows the Mach number distribution of the low-enthalpy test case (see also table 5-1: HEG-Low-E) as an example of the base flow calculations, including for the rear part a zoom of the grid.

The stability simulations obtained with the VESTA toolkit are based on mean flow computations with the second order finite volume solvers CFD++$^{®}$ (see for instance Peroomian and Chakravarthy [13]) and COOLFluiD (Lani *et al.* [14], Degrez *et al.* [15]). Grid convergence studies were conducted for each code as described in section 5.4.1.1.

The VirtusAero STABL software contains a structured, axisymmetric CFD solver, which solves the reacting Navier-Stokes equations and is maintained by Dr. Heath Johnson [16]. This flow solver is based on the finite-volume formulation. The inviscid fluxes are based on the modified Steger-Warming flux vector splitting method

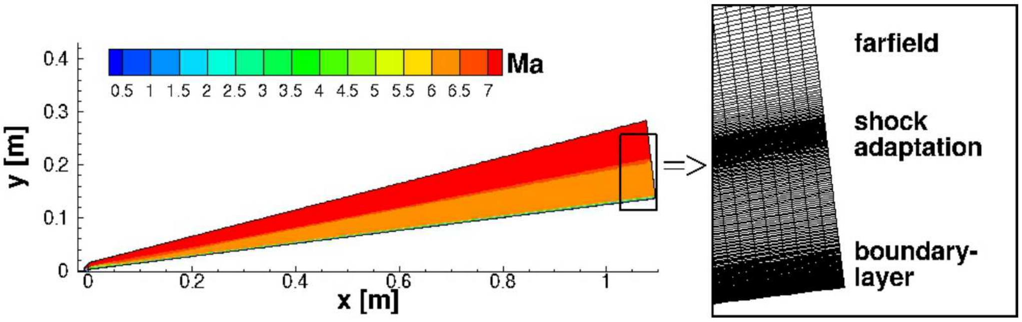

Figure 5-1: Example of Mean Flow: HEG-Low-E Test Case (CFD Solver: TAU).

and are second-order accurate with a MUSCL limiter as the TVD scheme. The viscous fluxes are second order accurate. The time integration method is the implicit, first-order DPLR method. The simulated gas is a mixture of ideal gases using N2, O2, NO, N, and O in chemical and thermal non-equilibrium. The viscosity law uses Blottner curve fit data for species viscosities and the Wilke mixing rule for mixture viscosity. The heat conductivity is calculated using Euckens relation.

5.3.2 LST / PSE Solver

The equations of the stability codes are derived from the conservation equations of mass, momentum and energy, which govern the flow of a viscous, compressible gas. All flow and material quantities are decomposed into a steady laminar base flow $\bar{q}$ and an unsteady disturbance flow $\tilde{q}$

$$q(x, y, z, t) = \bar{q}(x, y) + \tilde{q}(x, y, z, t). \tag{1}$$

The laminar mean flows $\bar{q}$ are calculated by different CFD codes (see previous section) and can be used without and with chemistry. The disturbance $\tilde{q}$ is represented as a harmonic wave

$$\tilde{q}(x, y, z, t) = \hat{q}(x, y) \exp[i(\alpha x + \beta z - \omega t)] + c.c. \tag{2}$$

with the complex-valued amplitude function $\hat{q}$.

The stability codes applied in this chapter are: the NOnLocal Transition analysis code (NOLOT [17]) of the German Aerospace Center, the Stability and Transition Analysis for hypersonic Boundary Layers code (STABL [16]) of VirtusAero and the VKI Extensible Stability and Transition Analysis (VESTA) toolkit [18], [19], [20] of the von Karman Institute. All codes can be used for Linear Stability Theory (LST) as well as Parabolized Stability Equations (PSE) analyses. Both approaches are applied in this chapter. In contrast to STABL and VESTA [21], which can account for real gas effects, NOLOT is limited to a calorically or thermally perfect gas.

The stability analyses performed using the STABL software suite are calculated with the PSE-Chem solver [16]. PSE-Chem solves the reacting, two-dimensional, axisymmetric, linear parabolized stability equations (PSE) to predict the amplification of disturbances as they interact with the boundary layer. The PSE-Chem solver includes finite-rate chemistry and translational-vibrational energy exchange.

The VESTA code is made of different components dealing with the different aspects of the stability equations solution: derivation of a generic set of equations, generation of an automated implementation and a set of solution algorithms associated to different ansatz. The toolkit has been tested against several cases available in the literature such as the one in Malik [22], Arnal [23] and Özgen and Kırcalı[24]. Several solvers are available within VESTA, namely LST, PSE and BiGlobal. They are all able to cope with different regimes from incompressible to compressible flows with LST and PSE dealing with chemical reactions.

5.4 RESULTS

Three test cases are chosen for the analyses of the chemical effects on the second mode: a low enthalpy experiment is conducted as reference case and two high enthalpy experiments as main test cases for the investigations of the chemical effects. See also table 5-1.

5.4.1 Low Enthalpy Test Case (HEG)

The chosen reference test case is an experiment, which was performed in HEG. This low enthalpy test case, HEG-Low-E, was conducted at a total enthalpy of 3.1 MJ/kg (table 5-1), at which the gas can be assumed to be calorically perfect.

5.4.1.1 Grid Convergence

Different axisymmetric grids are used for the base flow calculations: non-adapted grids as well as adapted grids. For the shock adapted grids with additional modulation of the outer grid limits, it is possible to reduce the number of points compared to the non-adapted grids. Apart from the number of grid points, also the wall normal distance of the first grid points has an effect.

Figure 5-2 shows the grid convergence study using the TAU code in combination with the NOLOT code. The calculated growth rates σ of the second mode is given as a function of the x-coordinate (axial distance measured from the blunt nose for this diagram as for all following pictures), for the described cone of section 5.2 and a comparable low-enthalpy free stream condition as HEG-LOW-E of table 5-1. Grid point clustering is applied towards the nose, the wall of the cone and the shock. Figure 5-2 demonstrates that the two finest grids deliver the same growth rates. For the following NOLOT investigations, the number of grid points is with about a half million between the two finest shown grids of figure 5-2.

Due to the use of different CFD solvers, the grid convergence study has to be done for each of them, separately. For the STABL code, Wagnild [25] summarized a detailed grid convergence study using a comparable geometry

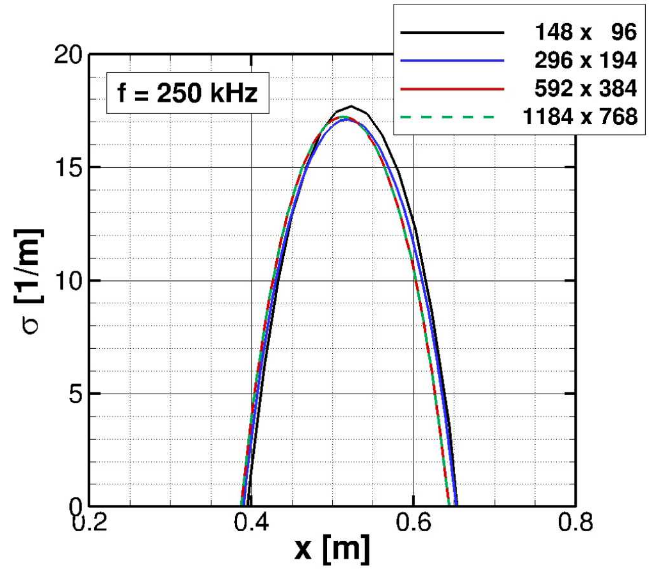

Figure 5-2: LST, NOLOT: $\sigma = \mathbf{f(x)}$ - Grid Convergence Study with Perfect Gas Assumption.

as well as comparable free stream conditions. Different grids up to a cell count of over 15 million cells were investigated. Based on these previous grid studies a grid of 1215 × 350 (about a half million grid points) is chosen. The following VESTA results based on a 1 million grid (2600 × 450). The VESTA grid study is summarized in Wartemann et al. [26].

5.4.1.2 Chemical Influence (HEG-Low-E)

In this subsection, PSE calculations performed with NOLOT are shown: in Figure 5-3a the calculated N-factors of the second mode as a function of the x-coordinate (axial distance measured from the blunt nose) for a frequency range from 200 up to 300kHz are depicted. The dashed lines in gray are based on perfect gas calculations, whereas the black lines are based on thermochemical non-equilibrium gas modeling (see also section 5.3.1). Almost identical results were obtained confirming the assumption of calorically perfect gas for the low enthalpy test case.

As mentioned in section 5.2, PCB sensors were used in the HEG experiments to measure the pressure fluctuations in the boundary layer, which are associated with second mode instabilities. From figure 5-3a the N-factors can be extracted at the transducer positions as shown in figure 5-3b for the three PCB sensor positions of the experiment. The calculated second mode is amplified in the streamwise direction. Due to the increase of the boundary layer thickness in the downstream direction and the relation between the boundary layer thickness δ and the second mode wavelength, $\lambda \approx 2\delta$, the typical shift towards lower frequencies can be observed.

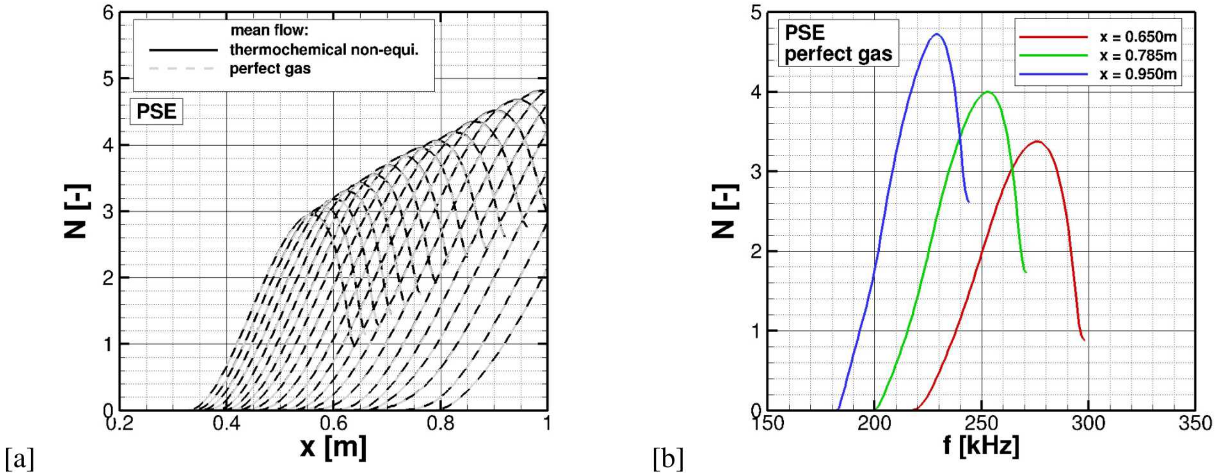

Figure 5-3: HEG-Low-E, PSE, NOLOT: a) N = f(x), b) N = f(f).

5.4.1.3 LST Comparison: VESTA / NOLOT (HEG-Low-E)

The first comparison of this section is visible in figure 5-4.a and illustrates the LST calculations of VESTA (dashed lines with symbols) and NOLOT (solid lines). To be consistent in the comparison the base flow as well as the LST calculations of both codes are based on the perfect gas assumption. The codes predict comparable results with small deviations: VESTA predicts slightly higher maximum N-factors while the frequency range shifts to higher values. Looking at the three maxima, for the N-factors as well as the frequencies, the discrepancy between both codes is less than 1.5%. This is an acceptable / typical deviation, using different mean flow solvers as well as LST solvers. The main reason for the differences is the application of different mean flow solver. Using the same grid and same mean flow solver (in this case: CFD++) delivers almost the same distributions, visible in figure 5-4.b. The small distinctions at the first and last maximum are caused by less extracted data points of the VESTA results for the maxima positions (the symbols marks the extracted data points of VESTA).

Figure 5-4.c demonstrates the effect of a physical model using a local thermodynamic equilibrium (LTE) approach. An LTE approach assumes the flow to be in a thermal and chemical equilibrium. For the VESTA base flow calculation the COOLFluiD code is applied, which uses the common LTE approach. That means all chemical reactions take place infinitely fast. To have a consistent LTE approach, the VESTA LST calculations are also based on the LTE assumption. Additionally, figure 5-4.c depicts the VESTA perfect gas outcome of figure 5-4.a/b (using CFD++ for the mean flow simulation). Of course, the expected differences between the VESTA results due to the different approaches are clearly visible in figure 5-4.c. The frequency range is similar, but the maximal N-factors show high deviations: the maximum N-factors compared to the perfect gas solution are about 15% lower.

Nevertheless, as already mentioned in section II, the HEG is a free-piston driven reflected shock tunnel with an expanded flow. The time required to reach an equilibrium condition, is defined by the density and local temperature. Therefore, depending on the ratio of the relaxation time to a characteristic timescale of the flow,

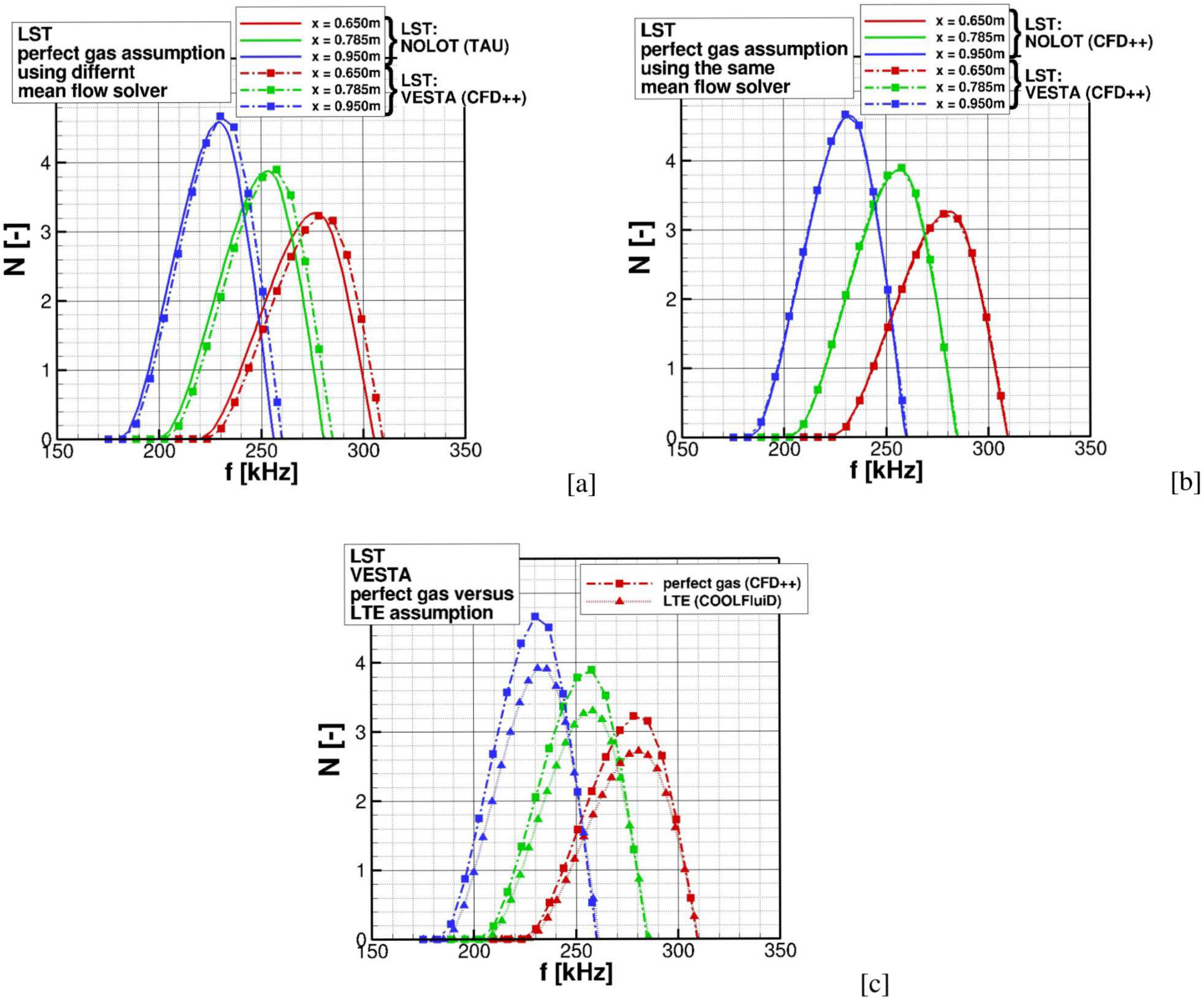

Figure 5-4: HEG-Low-E, LST, Comparison NOLOT and VESTA: N = f(f).

the chemical and thermal relaxation processes can be either in non-equilibrium or in equilibrium [4], depending on the test condition. For HEG test conditions with high enthalpy, a non-equilibrium approach is suggested for CFD calculations. For low enthalpy test cases, as the investigated case of this subsection, also a perfect gas approach is possible (see previous section 5.4.1.2).

5.4.1.4 PSE Comparison: STABL / NOLOT (HEG-Low-E)

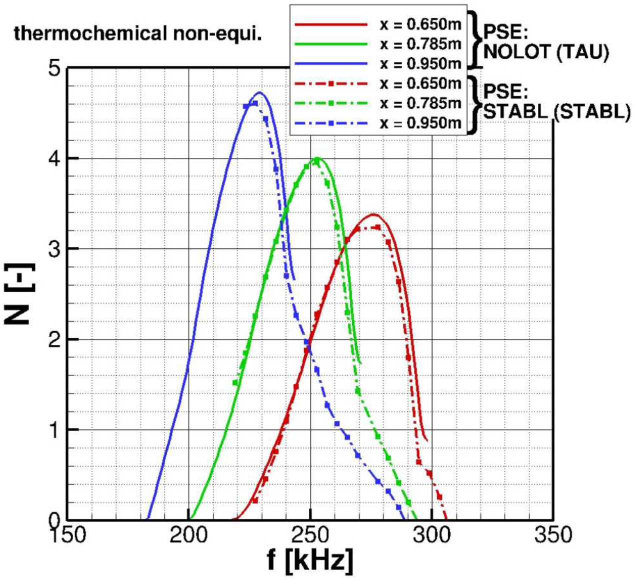

Figure 5-5: HEG-Low-E, PSE, Comparison NOLOT and STABL: N = f(f).

Previous investigations of the same geometry with a similar low enthalpy free stream condition, based on a comparison of the experimental / calculated growth rate of the second modes, show that it is possible to apply LST instead of PSE [27]. Nevertheless, LST neglects the nonparallel nature of the boundary layer as well as nonlinear effects. Thus, PSE is in general the preferable method.

The N-factor of the PSE calculations and consequently the differences between PSE and LST, depend on the chosen parameter for the PSE N-factor calculations, such as velocity or disturbance energy. For all PSE results in this chapter, the N-factors are derived based on the disturbance energy.

Figure 5-5 shows that the STABL results (dashed lines with symbols) are in a good agreement with the NOLOT calculations (solid lines). The mean flow as well as the stability calculations of STABL are performed with thermochemical non-equilibrium based on a two temperature approach. In contrast, due to the limitation of the NOLOT code, only the base flow simulation used thermochemical non-equilibrium. The differences between the code predictions are in the range of 1% comparing the maximum N-factors and the corresponding frequencies at the three sensor locations. These small deviation are in a similar range as these of the previous code to code comparison of section 5.4.1.3 (figure 5-4.a), which were mainly caused by the use of the distinct mean flow solvers and not caused by the use of different PSE solvers, or in case of figure 5-5, the use of different chemistry approaches for the stability calculations. Consequently, the results of fig. 5-5 confirmed, as expected for the low enthalpy case, the chemical effects are negligible.

5.4.1.5 Comparison to Experiment: HEG-Low-E

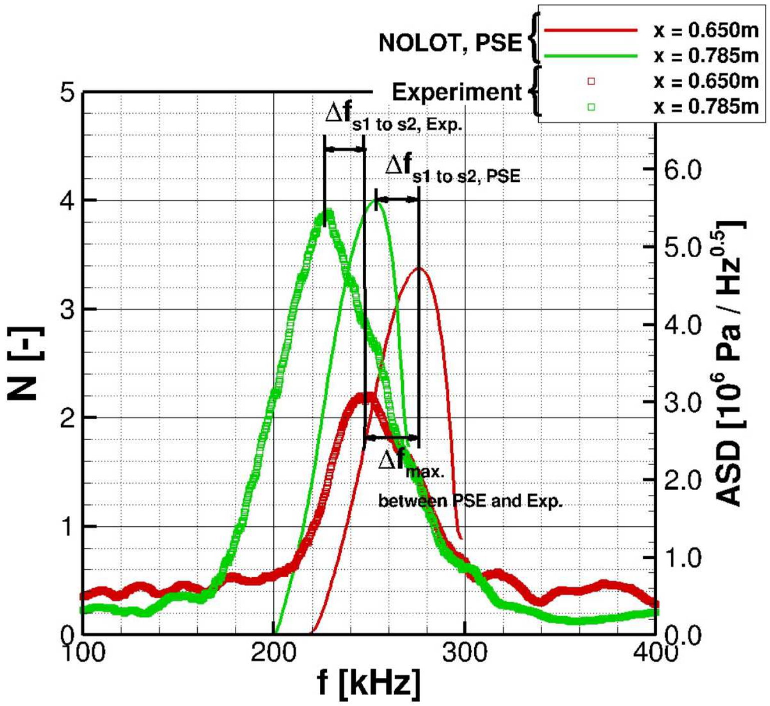

Figure 5-6: HEG-Low-E, Comparison NOLOT (N-factor) and Experimental Data (ASD).

For the second mode comparison of the numerical data with the measurements, two requirements are necessary. First, the second mode at the PCB sensor position has to be strong enough, meaning it has to be higher than the background noise level. Second, the flow at the sensor position has to be laminar. In the current case, the measured second mode at the last position (x = 950mm) is in the transition region. Thus, for the comparison with the measured second mode, the first and second sensor positions (x = 0.650 m, red color; x = 0.785 m, green color) are used. For the comparison with the experimental data, the results of the NOLOT code of the previous section are used.

Figure 5-6 shows the measured amplitude spectral density (ASD) marked as symbols. N-factors, which are based on PSE NOLOT calculations, as a function of the frequency are shown as lines. The differences of the peak frequencies are in the range of 10%. However, the frequency shift between the first and the second sensor positions is within about 22kHz for both the experiment and the computations, $\Delta f_{s1\ to\ s2,\ \mathrm{Exp.}} = \Delta f_{s1\ to\ s2,\ \mathrm{PSE}}$. Thus, a satisfactory agreement is observed, despite with a small frequency shift.

Several analyses were performed to investigate this frequency shift: Wagner et al. [28] investigated the influence of small deviations of the nose radius on the second mode. A change in the nose radius of 10% results in a frequency shift of about 10%. However, the nose is well proven for this test case. Further, Wagner et al. [28] investigated the influence of small variations of the angle of attack on the transition location and the second mode development. In two subsequent tests on the same model as used in the present study the angle of attack was varied in a range of $0.2°$, which a conservative estimation of angle of attack uncertainties. The analysis shows a negligible effect on the transition process and the second mode frequencies.

The good agreement in $\Delta f_{s1\ to\ s2}$ of the comparison makes small inaccuracies in the free stream condition the most likely reason for the Δf_{max}. In Wartemann et al. [29] the influence of usual measurement inaccuracies in the determination of the free stream conditions on the maximum frequency of the second modes are investigated using a $3°$ half-angle sharp cone. In reference [27], an investigation on the geometry used in the present study revealed, that a change of unit Reynolds number of about 5% results in a frequency shift of about 10%.

5.4.2 First High Enthalpy Test Case (HEG-High-E)

This section summarizes the comparison of the first high enthalpy test case: HEG-High-E with a total enthalpy of 11 MJ/kg.

5.4.2.1 PSE Comparison: STABL / NOLOT (HEG-High-E)

Figure 5-7 summarizes the PSE code to code analysis. The mean flow as well as the stability calculation of STABL, dashed lines with symbols, are performed with thermochemical non-equilibrium based on a two temperature model. For NOLOT (lines), different approaches are applied: data in Figure 5-7a are based on a calorically perfect gas assumption using a specific heat ratio of 1.4 for base flow as well as stability calculations. As expected, for the high enthalpy case major differences are visible. For all sensor positions a shift of the frequency range can be observed. Including chemistry reduces the boundary layer stability and increases the calculated N-factors. The deviations of the N-factors at the maximum of each sensor position between the two approaches depend strongly on the sensor position itself: for the first sensor, almost the same maximum N-factor is predicted, while for the second position, the deviation increases to a ΔN_{max} of around 10% and for the last sensor position up to over 10%. Figure 5-7b considers variations of the specific heat ratio. One result of the calculations of the complete nozzle is, that the specific heat ratio κ is reduced to 1.33. Using this reduced κ for the calorically perfect gas simulation delivers the values in Figure 5-7b. This numerical test approach does not affect the frequency range. Looking at the frequencies, the same differences between STABL and NOLOT as in figure 5-7a are visible. Due to the dependency on the position, the maximum N-factor at the first sensor position is overestimated from NOLOT, the second position is similar to the STABL results, and the last sensor is underestimated. Thus, only an upgrade to thermochemical non-equilibrium base flow simulations make senses, which is summarized in figure 5-7c. Minor differences between STABL and NOLOT are still visible especially for the downstream sensor positions. The differences of the N-factor at the maximum for the last sensor is about 3%. Consequently, real gas effects have a higher effect on the mean flow, than on the stability calculations itself. The application of the thermochemical non-equilibrium for the base flow in combination with the perfect gas assumption for the stability calculations result in a satisfactory agreement for the present test case. However, the

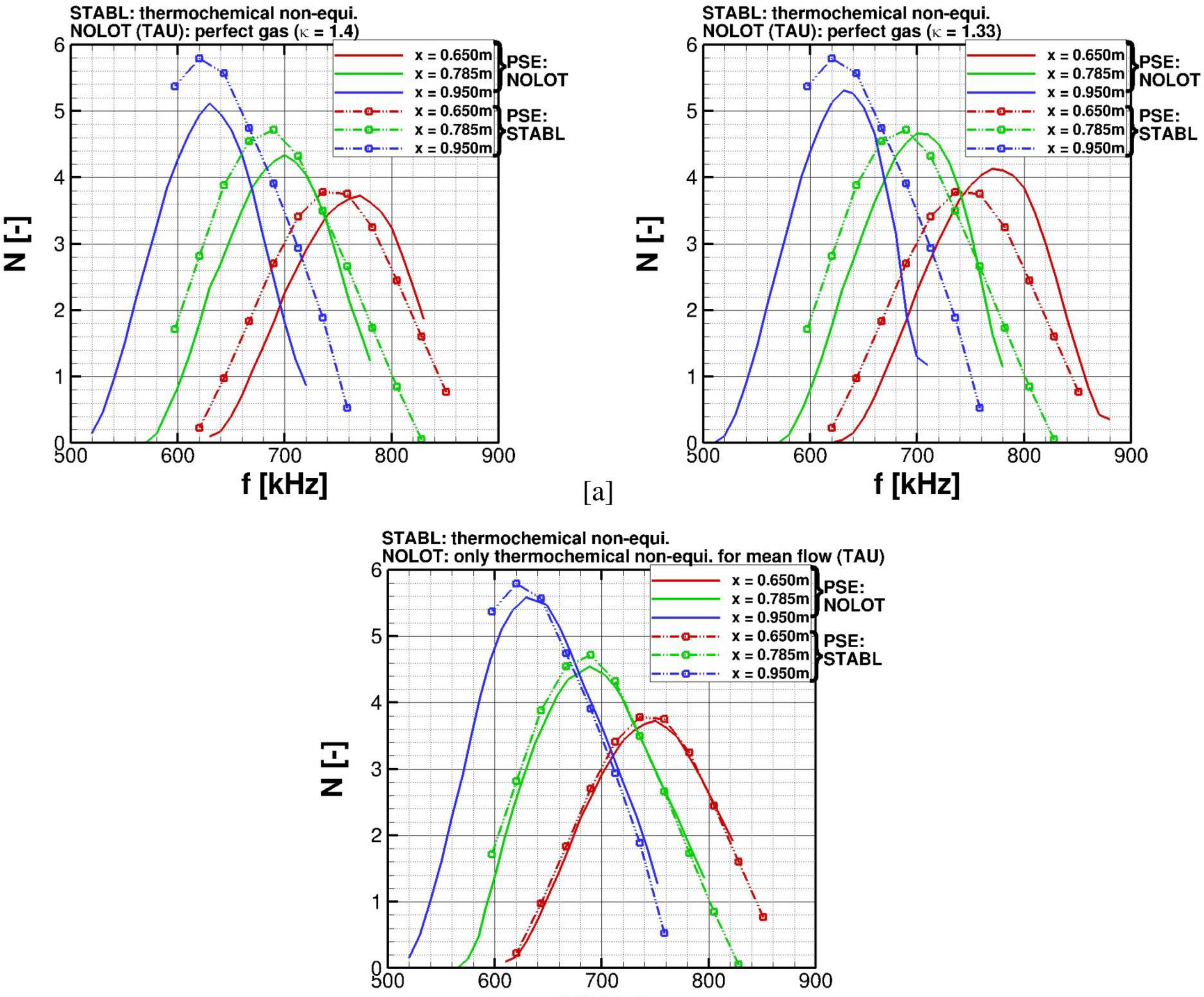

[a]

[b]

[c]

Figure 5-7: HEG-High-E, PSE, Comparison NOLOT and STABL: N = f(f).

error, due to the perfect gas assumption, propagates in streamwise direction and increases the discrepancy.

5.4.2.2 Comparison to Experiment: HEG-High-E

The code to code comparison of the previous section is based on a generic test case using the nominal free-stream conditions of table 5-1 to perform the simulations of the mean flow. For the comparison with the experimental data, the base flow simulation includes the nozzle, test camber and cone model.

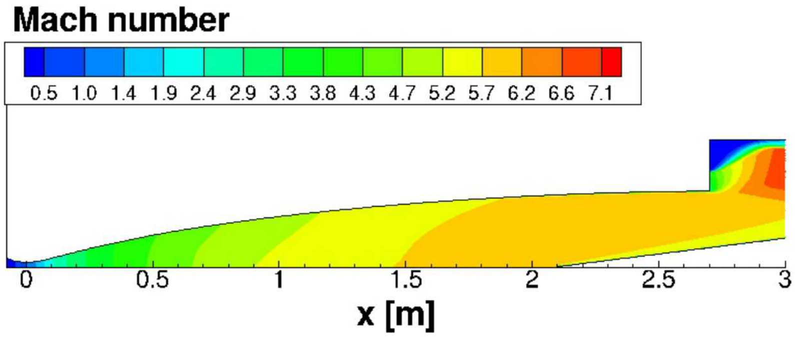

Figure 5-8: Base Flow Calculations of HEG-High-E Test Case (CFD Solver: TAU).

The grid is axially-symmetric and has about four million points clustered to the laminar walls and the shock. Based on the nozzle calibration of Wagner [9], the nozzle boundary layer is set turbulent. Due to the thermocouple measurements of the experiment, the boundary layer of the cone is known to be completely laminar. A thermochemical non-equilibrium approach based on a three temperature model is used. Figure 5-8 illustrates the Mach number distribution in the numerical nozzle - cone set up.

The second mode at the first PCB sensor position is not strong enough and still in the range of the background noise level. Thus, Figure 5-9 shows the measured amplitude spectral density (symbols) as function of the frequency for the second and third PCB sensor. The N-factors are based on NOLOT calculations using the mean flow simulation of figure 5-9.

The numerically predicted N-factor distribution is in relatively good agreement with the measured data, but with visible differences. Although the nozzle, the test section, and the cone model are simulated together, there are still uncertainties in the free stream conditions, which could explain the remaining differences. Nevertheless, the numerical results are in a satisfactory agreement with the experimental data.

5.4.3 Second High Enthalpy Test Case (HIEST-High-E)

This section summarizes the comparison of the second high enthalpy test case: HIEST-High-E with a total enthalpy of 10.9 MJ/kg. These test conditions for the second high-enthalpy case are chosen because of their

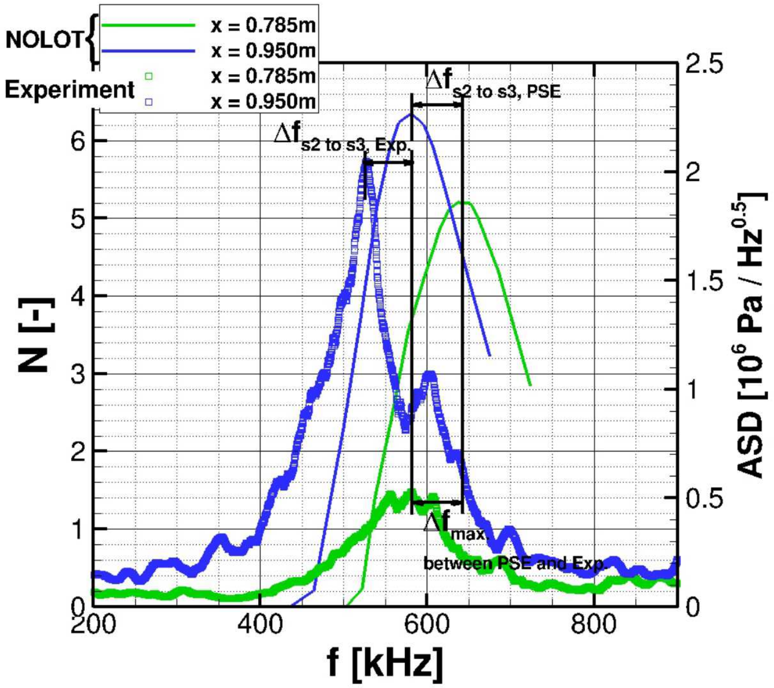

Figure 5-9: HEG-High-E, Comparison NOLOT (N-factor) and Experimental Data (ASD).

similarity to the HEG-High-E test case, with respect to unit Reynolds number, Mach number and total enthalpy.

5.4.3.1 PSE Comparison: STABL / NOLOT (HIEST-High-E)

Figure 5-10a summarizes the PSE code to code analysis. The mean flow as well as the stability calculations of STABL, dashed lines with symbols, are performed with thermochemical non-equilibrium based on a two temperature model. For NOLOT (solid lines) the mean flow is also simulated with the thermochemical non-equilibrium approach based on a two temperature model in combination with the perfect gas assumption for the NOLOT stability calculations. Due to the increase of the error in streamwise direction, which was described in section 5.4.2, the last sensor position was chosen for the code to code comparison to provoke the worst case with maximal deviation for the present test case.

The predicted frequency range is similar to the previous test case (HEG-HIGH-E) due to the similarity of the free stream conditions, the total enthalpy and the wind tunnel model. The difference of the maximum N-factors as well as the corresponding most amplified frequency between NOLOT and STABL are found to be approximately 3%. This confirms the validity of the selected approach for the NOLOT analyses.

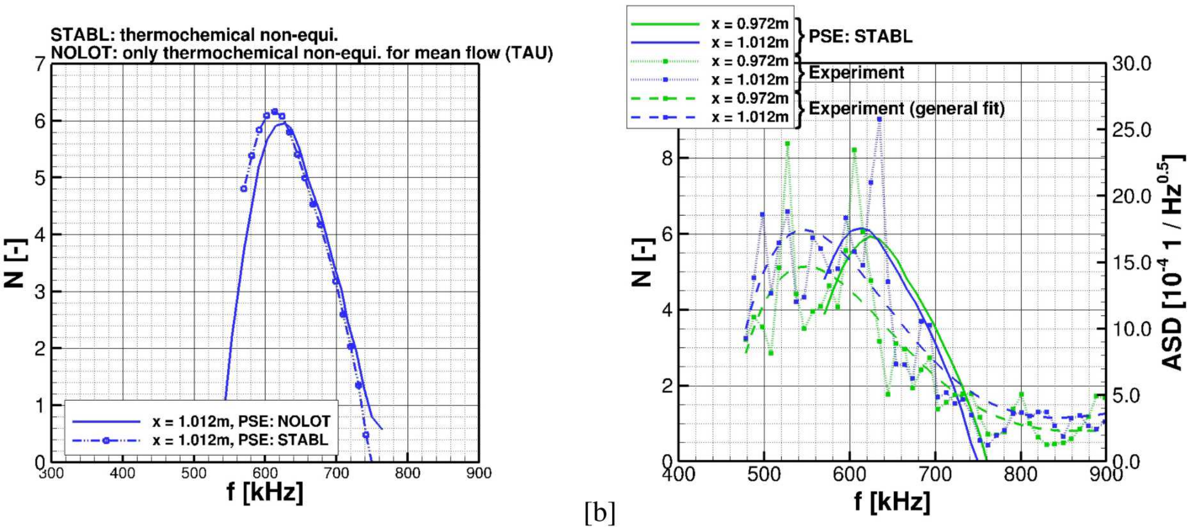

[a]

[b]

Figure 5-10: HIEST-High-E, Comparison a) NOLOT & STABL and b) STABL (N-factor) & Experimental Data (ASD).

5.4.3.2 Comparison to Experiment: HIEST-High-E

The last two sensor positions are chosen for the comparison conducted in this section.
Figure 5-10b shows the measured amplitude spectral density (ASD) marked as symbols. N-factors, which are based on PSE STABL calculations of the previous section, are shown as solid lines. The last two sensors of the HIEST-High-E case are with x = 0.972m and x = 1.012m very close together. Thus, the shift of frequencies due to the thickening of the boundary layer is only clearly visible for the stability results. The predicted frequencies of the second modes are in a similar frequency range as the experimental PCB data. Due to the scatter of the PCB data for this short-duration wind tunnel, the dashed lines show general fits of the ASD functions. Compared to the numerical data, the differences are about 10% for the frequencies at the maxima, which were already discussed in the previous section (see section 5.4.2).

5.5 CONCLUSION

In the scope of the present study different stability codes were compared: the NOnLocal Transition analysis code (NOLOT) of the German Aerospace Center (DLR), the Stability and Transition Analysis for hypersonic Boundary Layers code (STABL) of VirtusAero and the VKI Extensible Stability and Transition Analysis code (VESTA) of the von Karman Institute.

The code to code comparison revealed good agreement for the low enthalpy reference case. The deviations of the maximum N-factors and corresponding frequencies are around 1% and are expected to be mainly caused by using different CFD solvers for the mean flow computations. Since the gas can be considered being calorically perfect, the results obtained by using an thermochemical non-equilibrium approach for the mean flow and the stability code are almost identical to the approach of considering thermochemical non-equilibrium for the mean flow only.

The focus of this chapter is the high enthalpy test cases. The main results of the code to code comparison at high enthalpy are the following:

- Real gas effects reduce the boundary layer stability and thus increase the N-factors.
- If real gas effects are of importance, it is essential to model those in the mean flow computations.
- For the present test cases only minor effects, with acceptable errors, were observed considering or neglecting real gas effects in the stability analysis.
- Nevertheless, it is important to remember that errors can built up with increasing flow length.

The comparison to the experiments shows a good agreement to the numerical data regarding the predicted/measured frequency shift between two sensor position: for example: $\Delta f_{s1\ to\ s2,\ \mathrm{Exp.}} = \Delta f_{s1\ to\ s2,\ \mathrm{PSE}}$ was almost the same for the low enthalpy references case. The differences of the frequency at the maxima Δf_{max}, comparing the maximum N-factors with measured PCB data, are about 10%. Thus a satisfactory agreement is observed, despite with the mentioned frequency shift. Inaccuracies in the free stream conditions are the most likely reason for these deviations since the predicted N-factors are extremely sensitive towards small changes of the free stream condition and the corresponding base flow calculations.

5.6 ACKNOWLEDGEMENTS

Sandia National Laboratories is a multi-mission laboratory managed and operated by National Technology and Engineering Solutions of Sandia, LLC., a wholly owned subsidiary of Honeywell International, Inc., for the U.S. Department of Energy's National Nuclear Security Administration under contract DE-NA0003525.

5.7 REFERENCES

[1] Schneider, S., "Flight Data for Boundary Layer Transition at Hypersonic and Supersonic Speeds," *Journal of Spacecraft and Rockets*, Vol. 36, No. 1, 1999, pp. 8–20.

[2] Schneider, S., "Hypersonic Laminar-Turbulent Transition on Circular Cones and Scramjets Forebodies," *Process in Aerospace Sciences*, Vol. 40, No. 1-2, 2004, pp. 1–50.

[3] Mack, L.M., "Boundary layer linear stability theory," *AGARD - Special Course on Stability and Transition of Laminar Flow*, Vol. R-709, 1984, pp. 2–1 – 2–71.

[4] Hannemann, K., Martinez Schramm, J., and Karl, S., "Recent extensions to the High Enthalpy Shock Tunnel Göttingen (HEG)," *2nd International Atmospheric Reentry Association Days*, Arcachon, France, October 2008.

[5] Itho, K., Ueda, S., Komuro, T., Sato, K., Tanno, H., and Takahashi, M., "Hypervelocity Aerothermodynamic and Propulsion Research Using a High Enthalpy Shock Tunnel HIEST," *9th International Space Planes and Hypersonic Systems and Technologies Conference*, Vol. 12, 1999, pp. 93–98.

[6] Reimann, B. and Hannemann, V., "Numerical Investigation of Double-Cone and Cylinder Experiments in High Enthalpy Flows using the DLR TAU code," *48th AIAA Aerospace Sciences Meeting Including the New Horizons Forum and Aerospace Exposition*, 2010.

[7] Schwamborn, D., Gerhold, T., and Heinrich, R., "The DLR Tau-code: Recent Applications in Research and Industry," *European Conference on Computational Fluid Dynamics ECCOMAS CFD*, 2006.

[8] Mack, A. and Hannemann, V., "Validation of the Unstructured DLR-TAU-Code for Hypersonic Flows," *32nd AIAA Fluid Dynamics Conference and Exhibit*, St. Louis, Missouri, 24-26 June 2002, AIAA 2002-3111.

[9] Wagner, A., *Passive Hypersonic Boundary Layer Transition Control Using Ultrasonically Absorptive Carbon-Carbon Ceramic with Random Microstructure*, Ph.D. thesis, Katholieke Universiteit Leuven, 2014.

[10] Takahashi, M., Kodera, M., Itoh, K., Komuro, T., Sato, K., and Tanno, H., "Influence of thermal non-equilibrium on nozzle flow condition of high enthalpy shock tunnel HIEST," *AIAA Paper-2009-7267*, 2009.

[11] Tanno, H., Komuro, T., Sato, K., Itoh, K., and Takahashi, M., "Measurement of surface pressure fluctuation in hypersonic high-enthalpy boundary layer on a 7-degree cone model," *41st AIAA Fluid Dynamics Conference and Exhibit*, 2011.

[12] Wagner, A., Kuhn, M., Martinez Schramm, J., and Hannemann, K., "Experiments on passive hypersonic boundary layer control using ultrasonically absorptive carbon/carbon material with random microstructure," *Experiments in Fluids*, Vol. 54, 2013, pp. 1–10.

[13] Peroomian, O. and Chakravarthy, S., "A 'Grid-Transparent' Methodology for CFD," *35th Aerospace Sciences Meeting and Exhibit*, Reno,NV, 1997, AIAA 97-0724.

[14] Lani, A., Villedieu, N., Bensassi, K., Kapa, L., Panesi, M., and Yalim, M.S., "COOLFluiD: an open computational platform for multi-physics simulation," *21st AIAA Computational Fluid Dynamics Conference*, San Diego, CA, 2013, AIAA 2013-2589.

[15] Degrez, G., Lani, A., Panesi, M., Chazot, O., and Deconinck, H., "Modelling of high-enthalpy, high- Mach number flows," *Journal of Physics D: Applied Physics*, Vol. 42, 2009, pp. 1–16, Course Note 143.

[16] Johnson, H.B. and Candler, G.V., "Hypersonic boundary layer stability analysis using PSE-Chem," *35th AIAA Fluid Dynamics Conference and Exhibit*, Toronto, Ontario, Canada, 2005, AIAA Paper 2005-5023.

[17] Hein, S., Bertolotti, F.P., Simen, M., Hanifi, A., and Henningson, D., "Linear nonlocal instability analysis - the linear NOLOT code," Tech. Rep. IB-223-94 A56, DLR, 1994.

[18] Pinna, F., "VESTA toolkit: a Software to Compute Transition and Stability of Boundary Layers," *43rd Fluid Dynamics Conference, Fluid Dynamics and Co-located Conferences*, 2013.

[19] Pinna, F. and Groot, K., “Automatic derivation of stability equations in arbitrary coordinates and for different flow regimes,” *44th AIAA Fluid Dynamics Conference*, 2014.

[20] Pinna, F., *Numerical study of stability of flows from low to high Mach number*, Ph.D. thesis, Sapienza Università di Roma, 2012.

[21] Pinna, F. and P. Rambaud, P., “Linear Stability Analysis of Hypersonic Boundary Layer,” *7th Aerothermodynamics Symposium*, 2011.

[22] Malik, M.R., “Numerical methods for hypersonic boundary layer stability,” *Journal of Computational Physics*, Vol. 86, No. 2, 1990, pp. 376–413.

[23] Arnal, D., “Boundary Layer Transition: Special course on Progress in Transition Modelling,” *AGARD Report*, Vol. R-793, No. 761, 1994, pp. 2–1 – 2–61.

[24] Özgen, S. and Kırcalı, S., “Linear stability analysis in compressible, flat-plate boundary-layers,” *Theoretical and Computational Fluid Dynamics*, Vol. 22, 2008, pp. 1–20.

[25] Wagnild, R.M., *High Enthalpy Effects on Two Boundary Layer Disturbances in Supersonic and Hypersonic Flow*, Ph.D. thesis, University of Minnesota, 2012.

[26] Wartemann, V., Wagner, A., Wagnild, R., Pinna, F., Miró Miró, F., and Tanno, H., “Code to code comparison on hypersonic high enthalpy transitional boundary layers,” *2018 AIAA Aerospace Sciences Meeting*, Kissimmee, Florida, 2018, AIAA 2018-0351.

[27] Wartemann, V., *Mack-Moden-Dämpfung mittels mikroporöser Oberflächen im Hyperschall*, Ph.D. thesis, Technische Universität Braunschweig, 2014.

[28] Wagner, A., Hannemann, K., Wartemann, V., Tanno, H., and Ito, K., “Free piston driven shock tunnel hypersonic boundary layer transition experiments on a cone configuration,” *RTO - Hypersonic Laminar-Turbulent Transition Conference*, 2012.

[29] Wartemann, V., Lüdeke, H., Willems, S., and Gülhan, A., “Stability analyses and validation of a porous surface boundary condition by hypersonic experiments on a cone model,” *7th Aerothermodynamics Symposium*, Brugge, Belgium, 2011.